Chemistry and Physics of Lipids 233 (2020) 104989

Contents lists available at ScienceDirect

Chemistry and Physics of Lipids

journal homepage: www.elsevier.com/locate/chemphyslip

Adhesion and Aggregation of Spherical Nanoparticles on Lipid Membranes

Mohamed Laradji [a], P.B. Sunil Kumar [b], Eric J. Spangler [c]

[a] Department of Physics and Materials Science, The University of Memphis, Memphis, TN 38152, USA
[b] Department of Physics, Indian Institute of Technology Palakkad, Palakkad-668557, Kerala, India
[c] Department of Biomedical Engineering and Department of Physics and Materials Science, The University of Memphis, Memphis, TN 38152, USA

ABSTRACT

We present a review of recent results on the adhesion, wrapping and aggregation of spherical nanoparticles (NPs) on lipid membranes via molecular dynamics simulations of an implicit solvent model. We show that the degree of wrapping of small NPs, by tensionless planar membranes, can increase continuously with the adhesion strength. However, the degree of wrapping exhibits a discontinuity for large NPs or short interaction range. The adhesion of NPs to small vesicles, without volume constraint, also exhibits a discontinuity between weakly wrapped states and fully endocytosed states. Multiple spherical NPs, bound to tensionless planar membranes are either in a gas state, at weak adhesion strength, or aggregate, at relatively high adhesion strength, into a multitude of structures, corresponding to in-plane chains, out-of-plane tubes and rings, and out-of-plane single-chain tubes. Annealing scans and free energy calculations show that the gas and tube phases are the predominantly stable phases. In-plane chains are only stable for small aggregates and the out-of-plane bitubes are long-lived metastable states.

1. Introduction

Attractive forces between certain nanoparticles (NPs) and lipids leads to the adhesion of these NPs on the plasma membrane of living cells. This induces partial or full wrapping of the NPs by the membrane, and may result in their internalization through a process called endocytosis. Many studies have shown that NPs ability to be internalized by cells can potentially be utilized in a variety of biomedical applications, such as diagnostics Mieszawska et al. (2013), biosensing Anker et al. (2008), targeted drug delivery Sun et al. (2014), photothermal therapy Nel et al. (2009), magnetic hyperthermal therapy Périgo et al. (2015) and gene therapy Wang et al. (2016). To promote their uptake by specific cells, NPs that are designed for biomedical applications are typically coated with ligands to enhance their binding to specific receptors that are over-expressed on the plasma membranes of the targeted cells. Many studies have shown that non-specific binding and internalization of various types of NPs also occurs Chithrani et al. (2006), Tedja et al. (2012), He et al. (2014), Gao et al. (2017). Concerns have therefore also been raised in regard to the potential toxicity of many types of NPs Lewinski et al. (2009). The development of safe and effective NPs therefore requires a thorough understanding of their interaction with the plasma membrane. Since lipids are the main component of the plasma membrane, studies of how NPs interact with lipid bilayer membranes would therefore provide an important step toward a more comprehensive understanding of these interactions in the context of the more complex plasma membrane.

The adhesion of a spherical NP on a membrane, and the degree of wrapping of the NP by the membrane are a consequence of the interplay between the elasticity of the membrane and the adhesive forces between the NP and the membrane. In the particular case of a tensionless membrane and a contact adhesive interaction, the free energy of the system can be approximated by

$$F \approx -uA + 8\kappa\frac{A}{D^2}, \tag{1}$$

where A is the contact area between the membrane and the NP, $u(>0)$ is the adhesion energy per unit of area, κ is the membrane bending modulus, and D is the NP's diameter. From the minimization of this free energy, one finds that the NP binds to the membrane if u exceeds the threshold $u^* = 8\kappa/D^2$. Furthermore, since both terms in Eq. (1) are proportional to A, the NP is either completely wrapped by the membrane if $u > u^*$, or is completely unbound $u < u^*$. However, the NP is partially wrapped by a bilayer under finite tension, with the degree of wrapping that decreases with increasing tension. Several more refined continuum theories based on the Helfrich Hamiltonian Helfrich (1973) were developed in the context of planar membranes Deserno and Bickel (2003) and vesicles Deserno and Gelbart (2002), Raatz et al. (2014), Agudo-Canalejo and Lipowsky (2015). These theories typically assume contact NP-membrane interactions, implying that their validity is restricted to the limit of NPs that are much larger than the range of the interaction and the membrane thickness. These theories also neglect thermal fluctuations and assume that the elastic properties of the membrane are not locally renormalized by the bound NP.

Numerical methods provide an excellent tool in understanding

E-mail address: mlaradji@memphis.edu (M. Laradji).

https://doi.org/10.1016/j.chemphyslip.2020.104989
Received 30 May 2020; Received in revised form 2 October 2020; Accepted 2 October 2020

interactions between NPs and lipid membranes, particularly in the case of small NPs. Several studies of the interaction between NPs and lipid membranes have therefore been carried via a range of numerical methods, including Monte Carlo simulations, atomistic molecular dynamics and coarse-grained molecular dynamics simulations. For example, several Monte Carlo simulations of dynamically triangulated membranes, with elasticity described by the Helfrich Hamiltonian Helfrich (1973), have been performed in the past Saric and Cacciuto (2012, 2012 Bahrami et al. (2012). These models are however too coarse-grained and do not account for the local effect of the adsorbed NPs on the elasticity of the membrane. Several atomistic molecular dynamics simulations (AMD) have also been performed to investigate the adhesion of NPs on self-assembled lipid membranes Heikkilä et al. (2014), Lin and Alexander-Katz (2013), Van Lehn et al. (2013). Atomistic molecular dynamics simulations of NPs on lipid membranes are not computationally practical since the NPs lead to deformations of the membrane that extend well beyond the length scales that can be probed by this approach. Molecular dynamics of coarse-grained models of self-assembled lipid membranes have therefore been the most useful tool in elucidating the interactions between relatively small NPs and lipid membranes Vacha et al. (2011), Lin and Alexander-Katz (2013), Ruiz--Herrero et al. (2012), Spangler et al. (2016), Proskar et al. (2016). The adhesion of a NP on a lipid membrane leads to non-local curvature deformations of the membrane extending beyond the scale of the NP. As a result, the adhesion of two or more NPs may lead to overlapping curvature deformations, thereby inducing effective interactions between the NPs, and resulting in their aggregation on the membrane Koltover et al. (1999), van der Wel et al. (2016), Sarfati and Dufresne (2016), Sugikawa et al. (2016), Barbul et al. (2018). Similar effective interactions between NPs, but resulting from different physical mechanisms. For example, mixing NPs with homopolymers results in effective NP-NP interactions, which leads to a variety of NPs organizations including contact aggregates, bridging and telebridging aggregates, as well as sterically stable dispersions Hooper and Schweizer (2006). Interesting anisotropic aggregates of polymer-grafted NPs in the corresponding homopolymer matrix have also been observed Ackora et al. (2009), despite the isotropic nature of both the NPs and the matrix. Likewise mixing NPs with diblock copolymers can also lead to a rich phase behavior Lopes and Jaeger (2001), Kang et al. (2020). Effective NP-NP attractive forces are also induced when mixed with surfactants Jia et al. (2011), liquid crystals Rahimi et al. (2015), or when the particles are confined at fluid-fluid interfaces Kang et al. (2020), Niu et al. (2010).

Several theoretical attempts, based on the Helfrich Hamiltonian Helfrich (1973), were made in the past to determine the effective two-body and multi-body membrane-mediated interactions between membrane bound particles Goulian et al. (1993), Golestanian et al. (1996), Park and Lubensky (1996), Weikl et al. (1998), Evans et al. (2003), Yolcu et al. (2012). These theoretical investigations typically assume that the curvature deformations are weak, thereby allowing the calculations to be performed in the Monge gauge. Unfortunately, determining membrane-mediated interactions between NPs that induce strong curvature deformations requires the solution of non-tractable coupled non-linear partial differential equations. Therefore, here as well, simulations have played a major role in elucidating membrane-induced interactions between NPs and their ensuing self-assembly. Although AMD simulations have been performed to investigate the adhesion of single NPs on phospholipid membranes Heikkilä et al. (2014), Lin and Alexander-Katz (2013), Van Lehn et al. (2013), as stated earlier, AMD simulations of membranes with two or more NPs are very challenging since the AMD approach does not allow for simulations of large membranes over long time-scales. As a result, studies of membrane-mediated interactions between NPs have been carried mainly through simulations of coarse-grained models, such as Monte Carlo simulations of dynamically triangulated surfaces Saric and Cacciuto (2012, 2012, Bahrami et al. (2012), Ramakrishnan et al. (2013) as well as molecular dynamics of coarse-grained models Reynwar et al. (2007), Raatz et al. (2014), Olinger et al. (2016), Xiong et al. (2017), Angelikopoulos et al. (2017), Spangler et al. (2018).

In this article, we will review mostly prior results, based on an efficient implicit-solvent model of lipid membranes, introduced earlier by us Revalee et al. (2008), Laradji et al. (2016), for the investigation of the adhesion of single NPs on lipid membranes and their ensuing aggregation. In Section II, the model used in the studies is presented. In Section III, our main results of the adhesion of a single small spherical NP on tensionless planar membranes are reviewed and discussed Spangler et al. (2016), Spangler and Laradji (2020). In Section IV, we review our results on the effect of NP's size and range of interaction on their wrapping. In Section V, we present results on the wrapping of NPs by small vesicles. In Section VI, we review our main results on the self-assembly of spherical NPs on tensionless planar membranes Spangler et al. (2018). Finally, we conclude this article in Section VII.

2. Model and Computational Approach

The results presented in this review article are based on an implicit-solvent model in which a single molecule is coarse-grained into a semi-flexible linear trimer composed of one hydrophilic *h*-bead representing the lipid head group and two hydrophobic *t*-beads representing the lipid tail group. The potential energy of the lipid bilayer has three main contributions Revalee et al. (2008), Laradji et al. (2016):

$$U(\{\mathrm{r}_i\}) = \sum_{i,j} U^0_{\alpha_i\alpha_j}(r_{\mathrm{ij}}) + \sum_{\langle i,j\rangle} U_{\mathrm{bond}}(r_{\mathrm{ij}}) + \sum_{\langle i,j,k\rangle} U_{\mathrm{bend}}(\mathrm{r}_i,\mathrm{r}_j,\mathrm{r}_k), \tag{2}$$

where r_i is the coordinate of bead i, $\alpha_i(= h \text{ or } t)$ is the type of bead i, and $r_{\mathrm{ij}} = |\mathrm{r}_i - \mathrm{r}_j|$. In Eq. (2), $U_0^{\alpha\beta}$ is a soft piecewise two-body potential, between beads of types α and β, and is given by Laradji et al. (2016):

$$U^0_{\alpha_i\alpha_j}(r_{\mathrm{ij}}) = \begin{cases} (U^{\max}_{\alpha_i\alpha_j} - U^{\min}_{\alpha_i\alpha_j})\dfrac{(r_m - r_{\mathrm{ij}})^2}{r_m^2} + U^{\min}_{\alpha_i\alpha_j} & \text{if} \quad r_{\mathrm{ij}} \le r_m, \\ -2U^{\min}_{\alpha_i\alpha_j}\dfrac{(r_c - r_{\mathrm{ij}})^3}{(r_c - r_m)^3} + 3U^{\min}_{\alpha_i\alpha_j}\dfrac{(r_c - r_{\mathrm{ij}})^2}{(r_c - r_m)^2} & \text{if} \quad r_m < r_{\mathrm{ij}} \le r_c, \\ 0 & \text{if} \quad r_{\mathrm{ij}} > r_c, \end{cases} \tag{3}$$

where $U^{\max}_{\alpha\beta} > 0$ for any pair (α,β) and $U^{\min}_{\mathrm{hh}} = U^{\min}_{\mathrm{ht}} = 0$. Due to absence of explicit solvent in this model, the self-assembly of the lipids into stable bilayers is achieved by setting $U^{\min}_{\mathrm{tt}} < 0$ Laradji et al. (2016). In addition to $U^0_{\alpha_i\alpha_j}$, bonded beads within a single lipid chain also interact via the second term in Eq. (2), which is explicitly given by

$$U_{\mathrm{bond}}(r_{i,i+1}) = \frac{k_{\mathrm{bond}}}{2}(r_{i,i+1} - a)^2, \tag{4}$$

where k_{bond} is the stiffness of the bond and a is the preferred bond length. Finally, the third term in Eq. (2) maintains the stiffness of each lipid chain and is given by

$$U_{\mathrm{bend}}(\mathrm{r}_{i-1},\mathrm{r}_i,\mathrm{r}_{i+1}) = \frac{k_{\mathrm{bend}}}{2}(cos\theta_0 - \widehat{\mathrm{r}}_{i,i-1}\cdot\widehat{\mathrm{r}}_{i,i+1})^2, \tag{5}$$

where $\widehat{\mathrm{r}}_{i,j} = \mathrm{r}_{\mathrm{ij}}/r_{\mathrm{ij}}$, k_{bend} is the chains bending stiffness coefficient, and the preferred splay angle $\theta_0 = 180^o$. It is noted that beads belonging to the same lipid chain also interact with each other via Eq. (3), leading to an effective bond length that is slightly different from a. The interaction parameters of the lipid model are given by

$$\begin{aligned} U^{\rm hh}_{\rm max} &= U^{\rm ht}_{\rm max} = 100\varepsilon, \\ U^{\rm tt}_{\rm max} &= 200\varepsilon, \\ U^{\rm hh}_{\rm min} &= U^{\rm ht}_{\rm min} = 0, \\ U^{\rm tt}_{\rm min} &= -6\varepsilon, \\ k_{\rm bond} &= 100\varepsilon/r_m^2, \\ k_{\rm bend} &= 100\varepsilon, \\ r_c &= 2r_m \\ a &= 0.7r_m. \end{aligned} \tag{6}$$

In our studies, we used two NP models. In the first model (NP Model I) Hore and Laradji, 2007, 2008; Olinger et al., 2016; Spangler et al., 2016, a NP is constructed from the arrangement of n-beads in a face-centered cubic lattice. The beads belonging to a NP are bonded by the harmonic potential, $U_{\rm bond}$, given by Eq. (4) to maintain a rigidity and desired shape of the NP Spangler et al. (2016). The interaction parameters between the NP's n-beads, and between the NP and the lipid beads, are given by

$$\begin{aligned} U^{\rm nn}_{\rm max} &= U^{\rm nt}_{\rm max} = 100\varepsilon, \\ U^{\rm nh}_{\rm max} &= 200\varepsilon, \\ U^{\rm nn}_{\rm min} &= U^{\rm nt}_{\rm min} = 0, \\ U^{\rm nh}_{\rm min} &= -\mathcal{E}_I, \\ k_{\rm bond} &= 100\varepsilon/r_m^2 \text{ fortheNP}, \\ k_{\rm bend} &= 0 \text{ fortheNP}, \\ a &= 0.35r_m \text{ fortheNP}. \end{aligned} \tag{7}$$

In this model, the NP interacts attractively with the lipid head groups through $\mathcal{E}_I > 0$. The interaction between the NP and the lipid tail beads is however fully repulsive.

In NP Model I, a NP is described by a large number of degrees of freedom, making the model somewhat computationally inefficient, particularly in the case of many or large NPs. The description of isotropic spherical NPs can be made computationally more efficient by devising an alternative approach (NP Model II) in which the NP is modeled as a sphere with a uniform surface, and is therefore described by only the three degrees of freedom of its center of mass Spangler et al. (2018), Spangler and Laradji (2020). We note that this approach is however impractical in the case of NPs with anisotropic geometries or inhomogeneous surface properties Olinger et al. (2016). The two-body interaction between a lipid head or tail bead and an element of area of the NP's surface is of the same form as the two-body interaction given by Eq. (3). The net interaction between a lipid bead and a NP is obtained by integration over the NP's surface Spangler et al. (2018), Spangler and Laradji (2020), leading to Spangler and Laradji (2020)

$$U_{s\alpha}(r) = \begin{cases} 2\pi r_m'^2 \dfrac{R}{r}\left[\dfrac{A_{s\alpha}\left(R+r_m'-r\right)^4}{4r_m'^4} - \dfrac{A_{s\alpha}\left(R+r_m'-r\right)^3}{3r_m'^3} - \dfrac{u_{s\alpha}^{\rm min}\left(R+r_m'-r\right)^2}{2r_m'^2} + \dfrac{u_{s\alpha}^{\rm min}\left(R+r_m'-r\right)}{r_m'} + \dfrac{13u_{s\alpha}^{\rm min}}{20}\right] & \text{if } r \le R+r_m' \\ 2\pi r_m'^2 \dfrac{R}{r}\left[\dfrac{2u_{s\alpha}^{\rm min}\left(R+r_c'-r\right)^5}{5r_m'^5} - \dfrac{7u_{s\alpha}^{\rm min}\left(R+r_c'-r\right)^4}{4r_m'^4} + \dfrac{2u_{s\alpha}^{\rm min}\left(R+r_c'-r\right)^3}{r_m'^3}\right] & \text{if } R+r_m' < r \le R+r_c' \\ 0 & \text{if } r > R+r_c', \end{cases} \tag{8}$$

where $u_{s\alpha}^{\rm min}$ is the minimum value of the potential, per unit of area, between an element of area of the NP's surface and an h- or t-bead at a distance r_m'. $u_{s\alpha}^{\rm max} > 0$, $u_{\rm sh}^{\rm min} < 0$ and $u_{\rm st}^{\rm min} = 0$ to promote adhesion of the NP on the lipid membrane. In Eq. (8), $A^{s\alpha} = u_{\rm min}^{s\alpha} - u_{\rm max}^{s\alpha}$. The net interaction between two NPs is likewise calculated from the integration of the potential energies between two elements of the NP's surface. The interaction parameters of NP Model II are given by

$$\begin{aligned} u^{\rm sh}_{\rm max} &= u^{\rm st}_{\rm max} = 1210\varepsilon/r_m^2, \\ u^{\rm st}_{\rm min} &= 0, \\ u^{\rm sh}_{\rm min} &= -\mathcal{E}_{\rm II}, \\ r_c' &= 2r_m' = \lambda, \end{aligned} \tag{9}$$

with λ being the range of the interaction between the NP's surface and a lipid h-bead, and $\mathcal{E}_{\rm II}$ is the strength of the adhesion energy per unit of area. The relationship between the adhesion energies in NP Model I and II is about $\mathcal{E}_{\rm II} \approx 5\mathcal{E}_I/{\rm nm}^2$.

The beads in these studies are moved using a molecular dynamics approach with a Langevin thermostat Laradji et al. (2016), Spangler et al. (2018), and the equations of motion are integrated using the velocity-Verlet algorithm. Results discussed in this articles are based on simulations, with periodic boundary conditions in all directions, of tensionless planar membranes and of closed vesicles. Simulations based on vesicles are performed in the NVT ensemble. Simulations of planar membranes are performed in the NVTγ ensemble, where N is the total number of beads in the system, V is the volume of the system, T is temperature, and $\gamma = 0$ is the bilayer's lateral tension. The volume of the system is allowed to fluctuate using a Metropolis Monte Carlo scheme described in Refs. Spangler et al. (2016, 2018). All simulations are performed at $k_BT = 3.0\varepsilon$ with a time step $\Delta t = 0.02\tau$, where $\tau = r_m(m/\varepsilon)^{1/2}$.

3. Adhesion of a Single Spherical NP on Planar Lipid Membranes

A qualitative picture of the adhesion of a single NP on a planar tensionless lipid membrane is shown in Fig. 1, which depicts a series of snapshots, at equilibrium, for different values of the NP's diameter and adhesion strength. This figure demonstrates that the adhesion of a NP on the lipid membrane leads to the membrane's wrapping of the NP, with a degree of wrapping that increases with increasing the adhesion strength regardless of the NP's size. The degree of wrapping of the NP by the membrane is quantitatively defined as

$$Z = \frac{1}{2}(1 - cos\theta), \tag{10}$$

where the wrapping angle θ ($0 \le \theta \le \pi$). The NP is therefore unbound if $Z = 0$. However, The NP is completely wrapped if Z is almost 1. Note that due to the finite thickness of the bilayer, $Z < 1$, even for complete wrapping. In Fig. 2, the degree of wrapping for two NP sizes are shown as a function of adhesion strength. This figure confirms the qualitative results shown in Fig. 1, i.e. that the degree of wrapping increases with increasing adhesion strength, and that larger NPs are more easily wrapped by the membrane than small NPs.

The results above show that spherical NPs can be partially wrapped by tensionless membranes. This contradicts the argument, based on the minimization of the free energy in Eq. (1), predicting that a spherical NP is either unbound or completely wrapped by tensionless planar membranes. To confirm that the partially wrapped states shown in Fig. 1 are

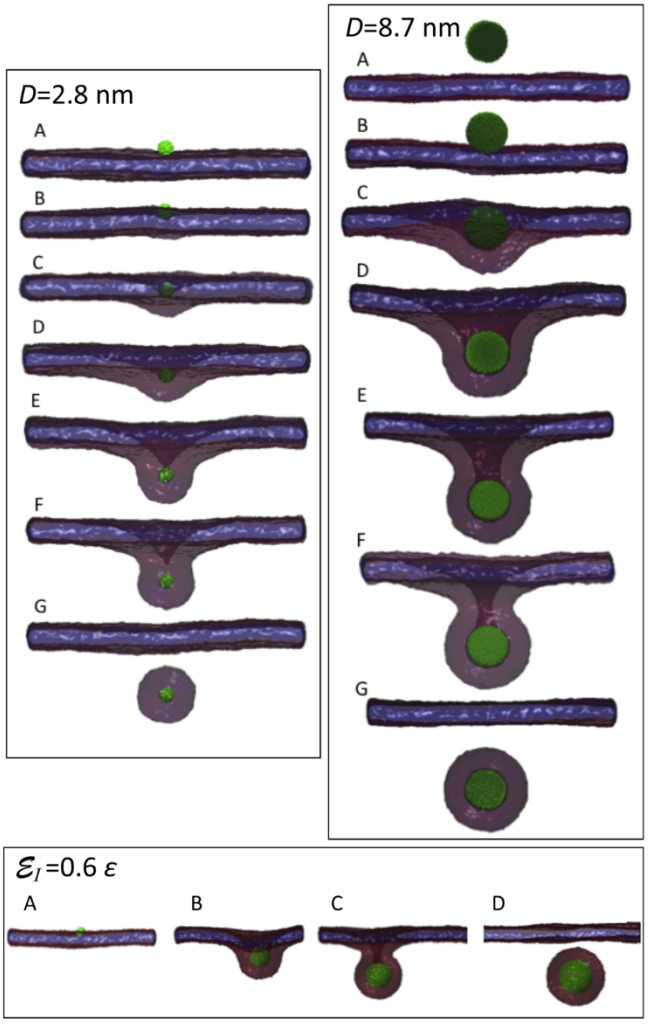

Fig. 1. Top left panel: Sequence of equilibrium snapshots of a NP (green) of diameter $D = 2.8$ nm with a tensionless bilayer. Snapshots A to G correspond to $\mathcal{E}_I = 0.6$, 1.0, 1.3, 2.0, 4.0, 6.5, and 7.0ϵ with $\epsilon = k_BT/3$, respectively, where $\mathcal{E}_I$ is the interaction strength between a bead belonging to the NP and a lipid head bead. Top right panel: Series of snapshots for the case of a NP with $D = 8.7$ nm. Snapshots A to G correspond to $\mathcal{E}_I = 0.01$, 0.40, 0.50, 0.60, 0.80, 0.90 and 1.0ϵ, respectively. Bottom panel: NPs of different diameters with a bilayer at $\mathcal{E}_I = 0.6\epsilon$. Snapshots A to D correspond to $D = 2.8$, 8.7, 11.5, and 14.4 nm, respectively. Note that when endocytosed, the NPs are encapsulated by a vesicle with the diameter of the inner leaflet about the size of the NP, as indicated by snapshots G for $D = 2.8$ and 8.7nm, and snapshot D in the bottom panel. Brown and blue represent the membrane and green correspond to the NP. Results based on NP Model I. Reproduced from Spangler et al. (2016).

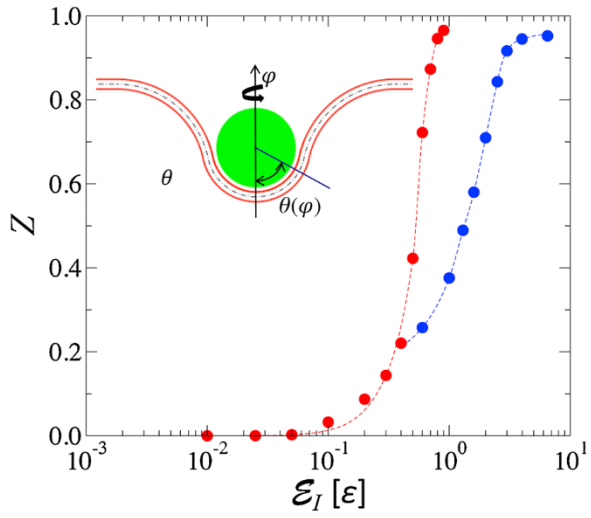

Fig. 2. Degree of wrapping, Z, defined by Eq. (10) and the inset diagram, vs adhesion strength for the case of $D = 8.7$nm (red symbols) and $D = 2.8$nm (blue symbols). Solid lines are guides to the eye. The wrapping angle θ is calculated as follows: For each azimuthal angle φ around the z-axis, a latitude angle $\theta_{max}(\varphi)$ is determined as the maximum latitude angle of lipid head beads within a distance $1.3r_m$ from the NP's surface. The wrapping angle θ is then determined from averaging θ_{max} over the azimuthal angle φ. Results based on NP Model I. Reproduced from Spangler et al. (2016).

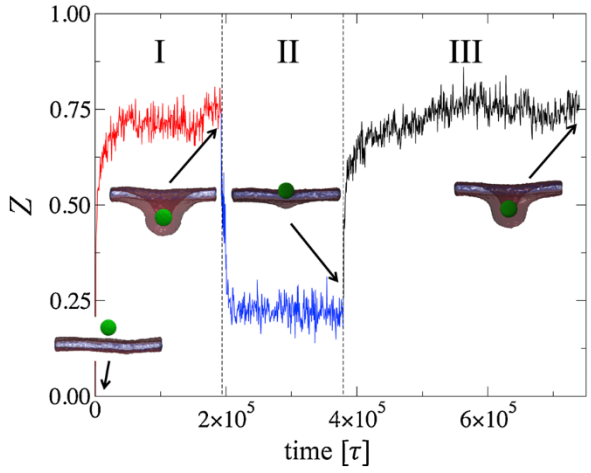

Fig. 3. The degree of wrapping, Z, vs time for a NP of diameter 8.7 nm. During stage I, $\mathcal{E}_I = 0.6\epsilon$, during stage II, $\mathcal{E}_I = 0.4\epsilon$, and during stage III, $\mathcal{E}_I = 0.6\epsilon$. The snapshots are final configurations in each stage. Results based on NP Model I. Reproduced from Spangler et al. (2016).

equilibrium and not metastable states, we performed the following sequence of simulations of a NP with diameter $D = 8.7$ nm, resulting in a degree of wrapping vs time shown in. Fig. 3. The system is initially equilibrated at a very low adhesion strength ($\mathcal{E}_I = 0.025\epsilon$), at which the NP is unbound. At the beginning of stage I, the adhesion strength is suddenly increased to 0.6ϵ, at which the system is let to equilibrate for almost $2\times 10^5\tau$. At this adhesion strength, the degree of wrapping $Z \approx 0.75$. At the end of stage I, the adhesion strength is then reduced to 0.4ϵ, and the system is let to equilibrate for almost $2\times 10^5\tau$ during stage II. During this stage, the degree of wrapping drops to $Z \approx 0.25$. Finally, at the beginning of stage III, the adhesion strength is increased back to 0.6ϵ. The degree of wrapping increases again back to its value during stage I, as shown in Fig. 3 . This simulation therefore confirms that the partially wrapped states of the NP are indeed equilibrium states and are independent of the initial configuration of the system.

We then determined the adhesion phase diagram, shown in Fig. 4, of a single NP with a tensionless membrane, as a function of NP's diameter and NP-membrane adhesion strength. Fig. 4 shows that there are three main phases corresponding to the unbound-NP phase for small values of adhesion strength (yellow region). This is followed by a phase at intermediate adhesion strengths where the NP is bound and partially wrapped by the membrane at intermediate values of $\mathcal{E}_I$ (green region). At high adhesion strength, the NP is endocytosed. The boundaries between the different phases decrease with increasing NPs' diameter, implying that it is easier for large NPs to adhere and be uptaken by a bilayer than small NPs. This agrees with Le Bihan *et al.*'s study, which showed that surface modified Au-NPs with diameters larger than 30 nm are spontaneously internalized by 1 μm liposomes, while smaller ones are not Le Bihan et al. (2009). We note that, here, the NP's uptake is spontaneous, and leads to the NP being completely wrapped by a vesicle with the

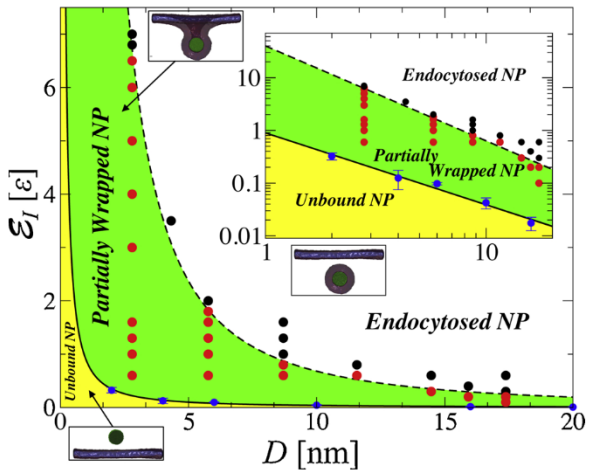

Fig. 4. Adhesion phase diagram of a spherical NP on a tensionless planar membrane. Black circles represent states where the NP is endocytosed. Red circles (green region) represent states where the NP is partially wrapped, and in the yellow region, the NP is unbound. Results based on NP Model I. Reproduced from Spangler et al. (2016).

inner diameter about that of the NP (see Fig. 1). There are other scenarios of NPs translocation through lipid membrane without engulfment, which can occur for example in the case of amphiphilic NPs Van Lehn and Alexander-Katz (2019) or hydorphobic NPs Ting and Wang (2012).

4. Effect of NP Size and Range of Interaction on their Adhesion on Planar Lipid Membranes

We recall that the minimization of the free energy based on the Helfrich Hamiltonian predicts that a spherical NP is either unbound or completely wrapped by a tensionless membrane Deserno and Bickel (2003). This theory assumes that the NP-membrane interaction is a contact interaction, and should therefore be valid only in the limit where the range of the interaction is much shorter than the size of the NP and the thickness of the bilayer. A more recent continuum theory by Raatz *et al.* Raatz et al. (2014), in which the range of the NP-membrane interaction is finite, shows that the degree of wrapping is continuous for any finite range of interaction, and that the particle is either unbound or completely wrapped by the membrane only in the limit of infinitesimally short-range interaction. Our computational results, shown in the previous section, were obtained from simulations of NPs with diameter less than 20 nm and range of NP-membrane interaction equal to 2 nm. To determine the effects of the size of larger NPs and range of interaction, we performed two sets of simulation using NP Model II; one with a fixed range of interaction $\lambda = 2$ nm and NP's diameter varying between 10 and 40 nm and another with a fixed diameter of 30 nm and range of interaction varying between 2 and 10 nm.

Fig. 5 shows that for NPs with diameter less than 20 nm, the degree of wrapping is continuous, in accord with our discussion in Section III using NP Model I. However, for $D \geq 20$nm, the degree of wrapping exhibits a discontinuity gap which increases with increasing D. Furthermore, if $D = 30$ and 40 nm, a hysteresis in the degree of wrapping is observed as the adhesion strength is scanned upward or downward, indicating that a first order wrapping transition emerges as the NP's diameter is increased.

The effect of range of interaction on the degree of wrapping is shown in Fig. 6 for the case of $D = 30$ nm. This figure shows that while the degree of wrapping exhibits some discontinuity up to $\lambda = 8$ nm, the increases of the degree of wrapping becomes continuous for $\lambda = 10$ nm. Figs. 5 and 6 show that a discontinuity in the degree of wrapping emerges as the NP's diameter is increased or as the range of interaction is decreased. Therefore, our simulations indicate that the theoretical limit, where the NP is either unbound (or marginally adhering to the membrane) or completely wrapped by the membrane should be asymptotically recovered from the simulations as D is increased or as λ is decreased Raatz et al. (2014).

5. NPs' Adhesion on Vesicles

The results presented above were focused on the adhesion of spherical NPs on tensionless planar membranes. It is of course useful to examine as well the adhesion of spherical NPs on vesicles, and determine the effect of the size of the vesicle on the degree of wrapping. We therefore also performed a series of simulations of 10-nm NPs on vesicles without volume constraint and with diameters corresponding to 32.8, 68.2, 90.8 and 106.3 nm. The degree of wrapping versus adhesion strength from these simulations, along with that for the case of a tensionless planar membrane, are shown in Fig. 7. This figure shows that the degree of wrapping is continuous for the case of the larger vesicles (90.8 and 106.3 nm), but then becomes discontinuous for the smaller ones (32.8 and 62.8 nm). The discontinuity in the degree of wrapping is

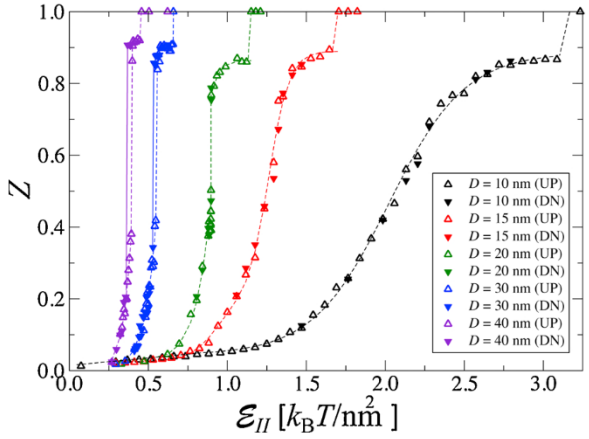

Fig. 5. Degree of wrapping vs adhesion strength for different NP's diameter and a range of interaction, $\lambda = 2$ nm. Black, red, green and blue correspond to $D = 10$, 15, 20, 30 and 40 nm, respectively. Open upward triangles correspond to upward annealing scans, whereas closed downward triangles correspond to downward annealing scans. Dotted and solid lines are guides to the eye. Results based on NP Model II. Reproduced from Spangler and Laradji (2020).

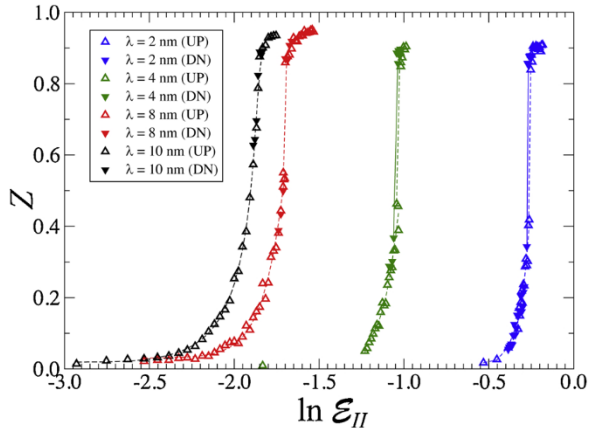

Fig. 6. Degree of wrapping vs adhesion strength for a 30-nm NP's and different values of the range of interaction, corresponding to $\lambda = 2$ nm (blue), 4 nm (green), 8 nm (red) and 10 nm (black). Open upward triangles correspond to upward annealing scans, whereas closed downward triangles correspond to downward annealing scans. Dotted and solid lines are guides to the eye. Results based on NP Model II. Reproduced from Spangler and Laradji (2020).

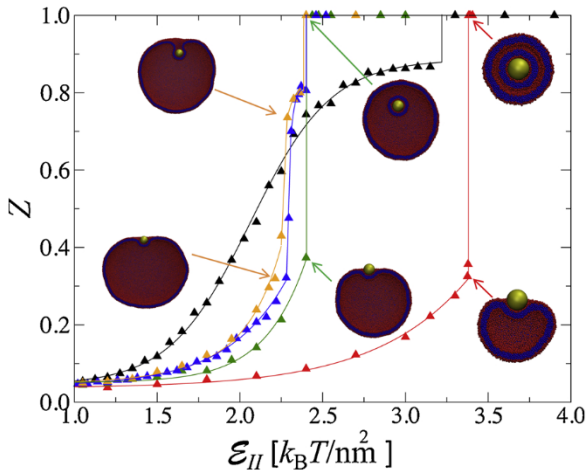

Fig. 7. Degree of wrapping of a 10-nm NP, vs adhesion strength, by vesicles with diameters corresponding to 32.8 nm (red), 68.2 nm (green), 90.8 nm (blue), and 106.3 nm (orange). Black symbols corresponds to the case of a planar membrane. Solid lines are guides to the eye. Results based on NP Model II.

however different from that for large NPs on planar membranes, discussed in the previous section (Fig. 5). In the case of large NPs on a planar membrane, the NPs experience a high degree of wrapping, albeit partial, at high adhesion strength. However, in the case of the 10-nm NP on small vesicles, when the degree of wrapping exhibits a discontinuity, the NP is either weakly wrapped or completely endocytosed.

6. Membrane-Induced Self-Assembly of Spherical NPs

The adhesion of a NP on a membrane leads to local deformations of the membrane that extend beyond the scale of the NP, as demonstrated by the configurations of Fig. 1 . This has the potential effect of inducing effective interactions between adhered NPs on the membrane, leading to their self-assembly.

To investigate the effect of NP's adhesion on their cooperative behavior on tensionless planar membranes, we first conducted a set of systematic simulations with two spherical NPs only Spangler et al. (2018). It is important to emphasize that, here, the direct interaction between the NPs is fully repulsive. Fig. 8 depicts the phase diagram of two NPs as a function of their diameter and the adhesion strength. This figure shows that for weak adhesion strength, the NPs are unbound, as expected. As the adhesion strength is increased, the NPs adhere to the membrane, while causing small local deformations in the membrane curvature, and their positions are spatially uncorrelated (G-phase in Fig. 8). As the adhesion strength is further increased, the amount of wrapping of each NP increases, leading to a gain in the adhesion energy at the cost of an increase in the membrane curvature energy. Beyond some adhesion strength, the curvature energy becomes too high to be compensated by the decrease in the adhesion energy for monomer NPs, leading to their dimerization into in-plane chains shown by a snapshot in Fig. 8 . With further increase of the adhesion strength, the in-plane dimers transform into out-of-plane dimers, or tubes, with a typical snapshot shown in Fig. 8, Finally, the NPs are endocytosed when the adhesion strength is further increased. This phase diagram demonstrates that despite the repulsive interaction between the NPs, effective attractive forces between them are induced by membrane deformations resulting from the adhesion of the NPs

In order to further understand the cooperative behavior of spherical NPs, induced by lipid membranes, we performed a series of simulations to obtain the aggregation phase behavior in terms of the number of NPs, N, on the membrane (i.e. their areal number density) and adhesion strength in the case of $D = 8$ nm. Fig. 9 shows this aggregation phase diagram obtained from slow upward annealing scans with respect to the adhesion strength. This figure demonstrates a rich phase behavior in which the size of the aggregate plays a major role. Snapshot configurations corresponding to the various phases in Fig. 9 are shown in Fig. 10.

Fig. 9 shows that for low adhesion strength, the NPs are randomly distributed on the membrane in a gas phase (snapshot A in Fig. 10). As the adhesion strength is increased from that in the gas phase, 2 to 5 NPs aggregate into chains (snapshots B and C in Fig. 10). However, as the adhesion strength is increased from the gas phase, for $N \geq 6$, the NPs aggregate into short-lived chains, which then transform into bitubular structures, shown by snapshot F in Fig. 10 . This bitube aggregate is made of two parallel out-of-plane chains in close proximity. A slice of a bitube along the xy-plane, shown by the right snapshot in panel F of Fig. 10, demonstrates that NPs are half wrapped in the xy-plane.

To further investigate the effect of the number of NPs in the aggre-

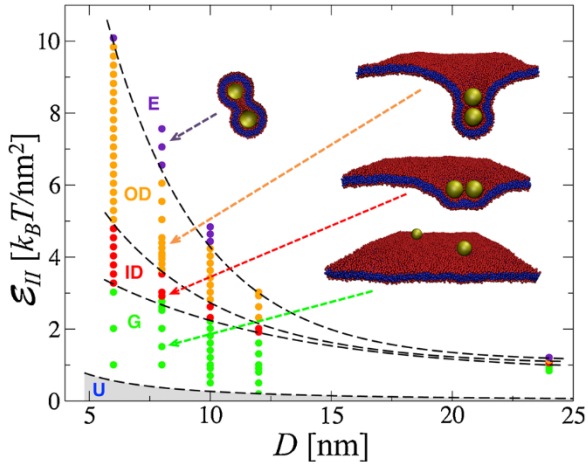

Fig. 8. Phase diagram of two NPs on a planar tensionless membrane, in terms of the NPs diameter and adhesion strength. Phases from bottom to top correspond to the unbound state (U-phase), the quasi-two-dimensional gas phase of bound NPs (G-phase), in-plane dimers (ID-phase), out-of-plane dimers or tubes (OD-phase) and endocytosed dimers (E-phase). Results based on NP Model II. Reproduced from Spangler et al. (2018).

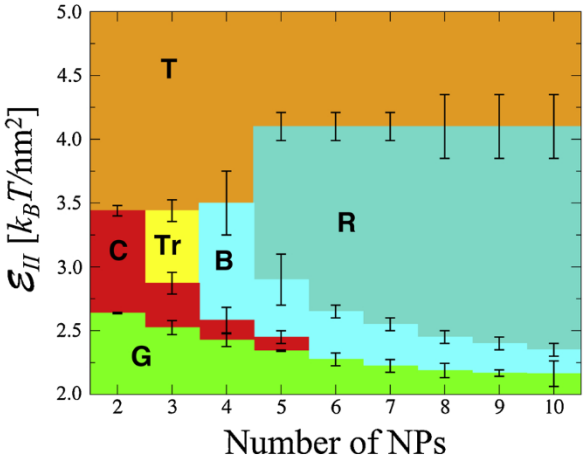

Fig. 9. Aggregation phase diagram in terms of the number of NPs and adhesion strength for the case of 8-nm NPs. G corresponds to the gas-phase (snapshot A in Fig. 10), C corresponds to the chain phase (snapshots B and C in Fig. 10), Tr corresponds to the trimer phase (snapshot D in Fig. 10), B corresponds to the bitube phase (snapshots E and F in Fig. 10), R corresponds to the ring phase (snapshots G in Fig. 10), and T corresponds to the tube phase (snapshots H and I in Fig. 10). Results based on NP Model II. Reproduced from Spangler et al. (2018).

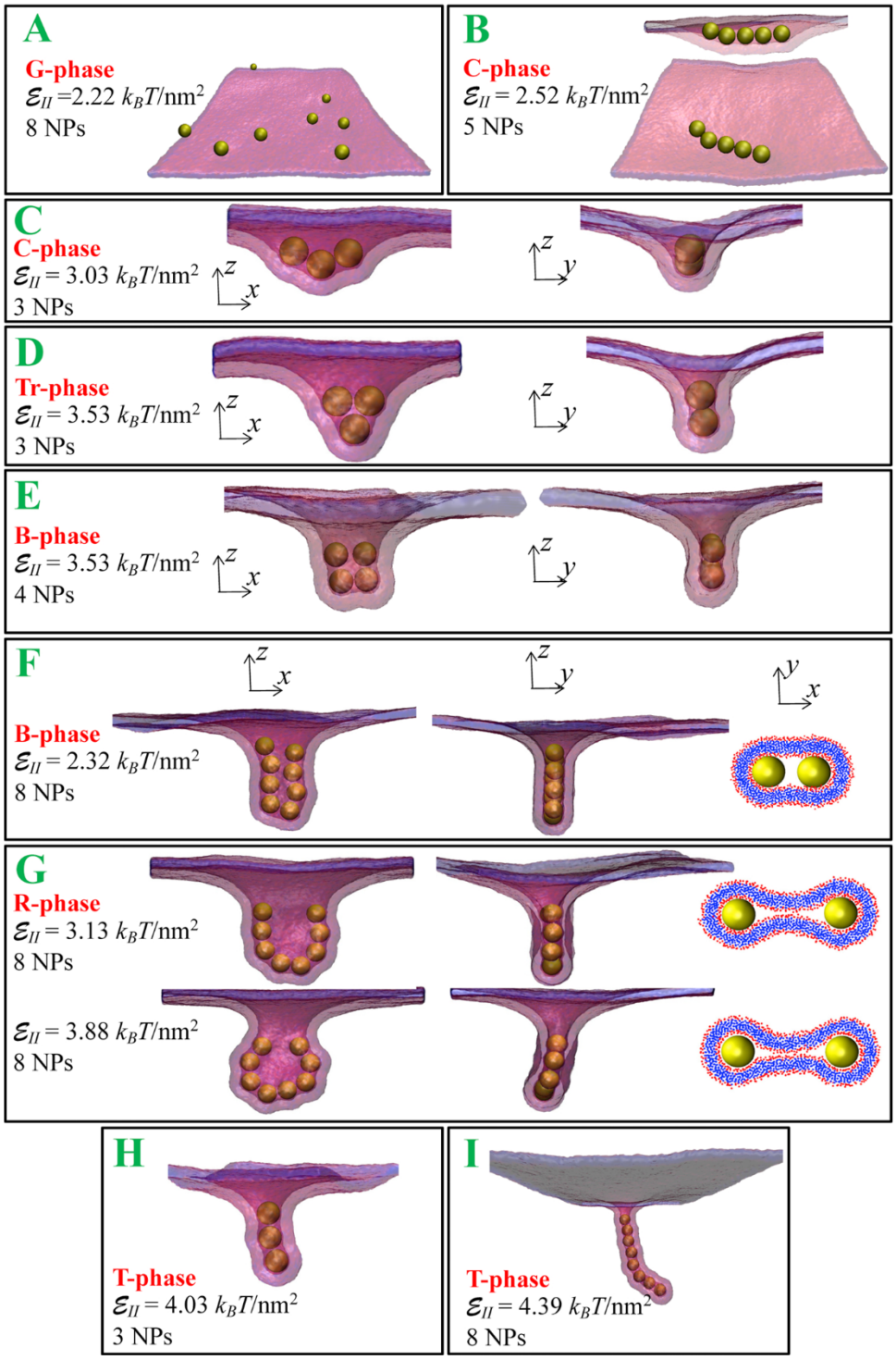

Fig. 10. Snapshots of the various aggregates. (A) Gas state of adsorbed NPs. (B) Two views of in-plane chains of 5 NPs. (C) Two views of in-plain chains of 3 NPs. (D) Different views of equilateral triangular cluster of 3 NPs. (E) and (F) Different views of bi-tube structures for 4 and 8 NPs, respectively. (G) Different views of the ring structure at two adhesion strengths for 8 NPs. (H) and (I) Tube structures of 3 and 8 NPs, respectively. Results based on NP Model II. Reproduced from Spangler et al. (2018).

gate on the stability of the chain phase, we conducted a series of simulations, where both adhesion strength and number of NPs are varied. The corresponding results are shown in Fig. 11 in terms of the number of contact lipids per NP versus time. Here, starting with 5 NPs in the gas phase at $\mathcal{E}_{II} = 2.32 k_BT/\text{nm}^2$, the adhesion strength is suddenly increased to $2.42 k_BT/\text{nm}^2$ leading to the spontaneous aggregation of the NPs into an in-plane chain (snapshot A in Fig. 11). The adhesion strength is then reduced back to $2.32 k_BT/\text{nm}^2$, leading to the dissociation of the chain into a gas (snapshot B in Fig. 11). Two additional NPs are then inserted into the system at random positions without change of the adhesion strength (snapshot C Fig. 11). The 7 NPs then spontaneously self-assemble into a chain (snapshot D in Fig. 11). However, this chain is short-lived, and eventually transforms into a bitube (snapshot E in Fig. 11). This simulation shows that while the chain structure seem to be stable for $N = 5$, it is actually unstable, or at best metastable, for $N = 7$. In contrast, the addition of NPs to a bilayer with a bi-tube or ring aggregate does not destabilize the structure.

For $N \leq 5$, further transformation of the chain structure, with increasing adhesion strength, depends on the number of NPs. We have seen earlier that 2-NPs chains transform into out-of-plane tubes, shown in Fig. 8 . However, 3-NPs chains (snapshot C in Fig. 10) transform into out-of-plane equilateral triangular trimers (snapshot D in Fig. 10). 4- and

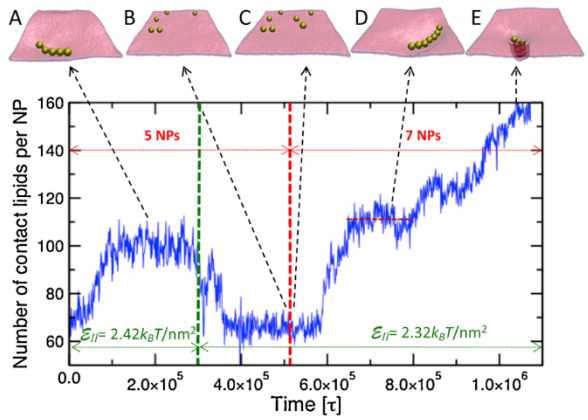

Fig. 11. The number of lipids in contact with the NPs, normalized by the number of NPs, vs time, as both $\mathcal{E}_{II}$ and N are varied. To the left and right of the vertical dashed green line, the adhesion strength is 2.42 and 2.32k_BT/nm^2, respectively. To the left and right of the vertical dashed red line, $N = 5$ and 7, respectively. Snapshots A to E show the configuration of the NPs in each stage of the simulation. Results based on NP Model II. Reproduced from Spangler et al. (2018).

5-NPs chains, however, transform into bitubes (snapshot E in Fig. 10). For $N \geq 5$, the bitube structure evolves into a ring, shown by snapshots G in Fig. 10 . The evolution of the bitube structure into a ring is due to the increased degree of wrapping each NP experiences with increasing the adhesion strength, as demonstrated by the right snapshots in panel G of Fig. 10 . Since rings necessitate at least 5 NPs, they are not observed in the case of smaller aggregates. As the adhesion strength is further increased, all aggregates transform into out-of-plane tubes shown by snapshots H and I for $N = 3$ and 8, respectively. The in-plane linear

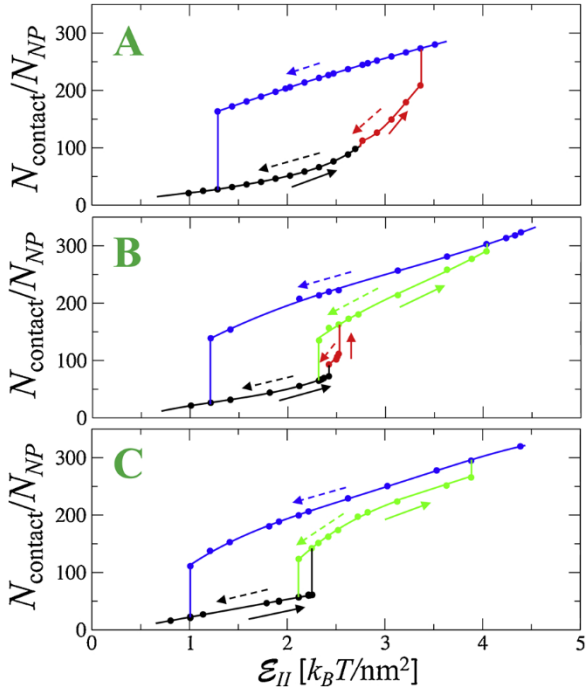

Fig. 12. Number of lipids, per NP, that are in contact with NPs, vs adhesion strength for the case of $N = 2$ (A), $N = 5$ (B) and $N = 8$ (C). Data obtained from upward annealing scans (solid arrows) and downward annealing scans (dashed arrows). Black curves correspond to the gas phase, red curves correspond to the in-plane chain phase, green curves correspond to the bitube/ring phase, and the blue curves correspond to the out-of plane tube phase. Results based on NP Model II. Reproduced from Spangler et al. (2018).

chains (C-phase) and out-of plane chains (T-phase) were observed by Saric and Cacciuto Saric and Cacciuto (2012) using the dynamic triangulation Monte Carlo model Sunil Kumar and Rao (1998).

To further infer the stability of the various observed structures, we performed both upward and downward annealing scans with respect to the adhesion strength. The obtained numbers of contact lipids, per NP, versus $\mathcal{E}_{II}$ are shown for the cases of $N = 2$, 5 and 8 in Fig. 12. All upward annealing scans start from the gas phase. This figure shows that for both cases of 2 and 5 NPs, the transition from the gas phase to the chain phase is reversible. The transition from the gas phase to the bitube phase, in the case of the 8 NPs is characterized by a hysteresis. Interestingly an annealing downward from the bitube phase leads always to the gas phase, with the in-plane chain phase being completely bypassed. Likewise, downward annealing from the tube phase always leads to the gas phase, bypassing all other structures, regardless of the size of the aggregate. Therefore, there exist high energy barriers between the tube phase and the bitube/ring phase as well as between the tube phase and the chain phase, which might prevent the system from reaching equilibrium.

Free energy calculations would be very useful in determining the stability of the various observed structures. Free energy calculations using the potential of mean force in conjunction with the weighted histogram analysis method Kumar et al. (1992) would be desirable. However, this approach is not practical in this case as it requires non-trivial reaction coordinates. We therefore opted for an alternative approach that provides an approximate free energy

$$\mathcal{F} = E_{\text{adh}} + \mathcal{F}_{\text{curv}}, \tag{11}$$

where E_{adh} is the adhesion energy and $\mathcal{F}_{\text{curv}}$ is calculated using a local Monge representation of the Helfrich Hamiltonian Helfrich (1973) for the determination of the membrane curvature contribution to the free energy, as detailed in Ref. Spangler et al. (2018). We note that this is a saddle-point approximation accounting mostly for configurations of the membrane around the minimum of the free energy. Eq. (4) does not therefore fully account for the conformational entropy of the lipid membrane. The calculations show that the gas and tube phase are predominantly stable phases over wide intervals of adhesion strength. The chain phase is found to be stable over a narrow range of adhesion strength for five or less NPs only. The bitube phase, on the other hand is only marginally stable for a very narrow range of adhesion strength.

7. Conclusions

In this article, we reviewed recent results, based on molecular dynamics simulations, of NPs adhesion and self-assembly on lipid membranes. The solvent is implicit in this model and the interactions are soft. These allows for systematic and large scale simulations over a wide range of NPs diameter, their number, and adhesion strength. We found that the degree of wrapping, of NPs adhering to tensionless planar membranes, increases continuously with increasing the adhesion strength for small NPs. However, for larger NPs, we found that the degree of wrapping exhibits a discontinuity with a gap that increases with increasing the adhesion strength. We also found that the discontinuity for the larger NPs disappear as the range of interaction is increased. The results of the continuum theory based on the minimization of the Helfrich Hamiltonian only explores a limited regions of the phase diagram, which is recovered by the method used here Deserno and Bickel (2003). Our approach demonstrates that the actual phase diagram is much richer than predicted by the continuum theory.

In the case of NPs bound to vesicles without volume constraint, we found that the degree of wrapping for small NPs increases continuously with adhesion strength for large vesicles, it also exhibits a discontinuity for small vesicles. Here, the discontinuity is between weakly wrapped states and endocytosed states.

Our investigation of the many NPs bound to tensionless planar

membranes shows a rich aggregation phase diagram that depends strongly on the size of the aggregate and the adhesion strength. For weak adhesion strength, the NPs are in a quasi-two-dimensional gas state. As the adhesion strength is increased, in-plane chains are observed for aggregates composed of a small number of NPs. However, aggregates composed of a larger number of NPs transform into out-of plane bitubes, corresponding to two apposed parallel out-of-pane chains. As the adhesion strength is further increased, the bitubes transform into out-of-plane rings. For even higher adhesion strength, the NPs aggregate into out-of-plane single chain tubes. Free energy calculations and annealing scans with respect to the adhesion strength show that the gas phase and the out-of-plane tubes are the predominant phases. The in-plane chains and the bitube/ring structures appear only during upward annealing with respect to adhesion strength. They are however, completely absent during downward annealing scans. Free energy calculations show as well that the chain phase appear to be stable for a very narrow range of adhesion strength and small aggregates. The bitube structure is at best marginally stable over a narrow range of adhesion strength.

Acknowledgements

This work was partially supported by the National Science Foundation (DMR-1931837) and by a Faculty Research Grant from the University of Memphis. The later support does not necessarily imply endorsement by the University of the present research conclusions. All simulations were performed on computers of the High Performance Computing Facility of the University of Memphis. All snapshots in this article were generated using VMD version 1.9.3 Humphrey et al. (1996).

References

Mieszawska, A.J., Mulder, W.J.M., Fayad, Z.A., Cormode, D.P., 2013. Multifunctional gold nanoparticles for diagnosis and therapy of disease. Mol. Pharmaceutics 10, 831–847.
Anker, J.N., Hall, W.P., Lyandres, O., Shah, N.C., Zhao, J., Van Duyne, R.P., 2008. Biosensing with plasmonic nanosensors. Nat. Mat. 7, 442–453.
Sun, T., Zhang, Y.S., Pang, B., Hyun, D.C., Yang, M., Xia, Y., 2014. Engineered nanoparticles for drug delivery in cancer therapy. Angew. Chem. Int. Ed. Engl. 53, 12320–12364.
Nel, A.E., Mäder, L., Velegol, D., Xia, T., Hoek, E.M.V., Somasundaran, P., Klaessig, F., Castranova, V., Thompson, M., 2009. Understanding biophysicochemical interactions at the nano-bio interface. Nat. Mat. 8, 543–557.
Périgo, E.A., Hemery, G., Sandre, O., Ortega, D., Garaio, E., Pazaola, F., Teran, F.J., 2015. Fundamentals and advances in magnetic hyperthermia. Appl. Phys. Rev 2, 041302.
Wang, K., Kievit, F.M., Zhang, M., 2016. Nanoparticles for Cancer Gene Therapy: Recent Advances, Challenges, and Strategies. Pharmacol. Res. 114, 56–66.
Chithrani, B.D., Ghazani, A.A., Chan, W.C.W., 2006. Determining the size and shape dependence of gold nanoparticle uptake into mammalian cells. Nano Lett. 6, 662–668.
Tedja, R., Lim, M., Amal, R., Marquis, C., 2012. Effects of serum adsorption on cellular uptake profile and consequent impact of titanium dioxide nanoparticles on human lung cell lines. ACS Nano 5, 4083–4093.
He, Z., Liu, J., Du, L., 2014. The unexpected effect of PEGylated gold nanoparticles on the primary function of erythrocytes. Nanoscale 6, 9017–9024.
Gao, X.L., Yue, T.T., Tian, F.L., Liu, Z.P., Zhang, X.R., 2017. Erythrocyte membrane skeleton inhibits nanoparticle endocytosis. AIP Adv 7, 065303.
Lewinski, N.V., Colvin, V., Drezek, R., 2009. Cytotoxicity of nanoparticles. Small 4, 26–49.
Helfrich, W., 1973. Elastic properties of lipid bilayers: Theory and possible experiments. Z. Naturforsch. 28, 693–703.
Deserno, M., Bickel, T., 2003. Wrapping of a spherical colloid by a fluid membrane. Europhys. Lett. 62, 767–773.
Deserno, M., Gelbart, W.M., 2002. Adhesion and wrapping in colloid-vesicle complexes. J. Phys. Chem. B 106, 5543–5552.
Raatz, M., Lipowsky, R., Weikl, T.R., 2014. Cooperative wrapping of nanoparticles by membrane tubes. Soft Matter 10, 3570–3577.
Agudo-Canalejo, J., Lipowsky, R., 2015. Critical Particle Sizes for the Engulfmentof Nanoparticles by Membranes andVesicles with Bilayer Asymmetry. ACS Nano 4, 3704–3720.
Saric, A., Cacciuto, A., 2012a. Fluid membranes can drive linear aggregation of adsorbed spherical nanoparticles. Phys. Rev. Lett 108, 118101.
Saric, A., Cacciuto, A., 2012b. Mechanism of membrane tube formation Induced by adhesive nanocomponents. Phys. Rev. Lett 109, 188101.
Bahrami, A.H., Lipowsky, R., Weikl, T.R., 2012. Tubulation and aggregation of spherical nanoparticles adsorbed on vesicles. Phys. Rev. Lett 109, 188102.
Heikkilä, E., Martinez-Seara, H., Gurtovenko, A.A., Javanainen, M., Häkkinen, H., Vattulainen, I., Akola, J., 2014. Cationic Au nanoparticle binding with plasma membrane-like lipid bilayers: Potential mechanism for spontaneous permeation to cells revealed by atomistic simulations. J. Phys. Chem. C 118, 11131–11141.
Lin, J., Alexander-Katz, A., 2013. Cell Membranes open doors for cationic nanoparticles/biomolecules: Insights into uptake kinetics. ACS Nano 7, 10799–10808.
Van Lehn, R.C., Atukorale, P.U., Carney, R.P., Yang, Y.S., Stellaci, F., Irvine, D.J., Alexander-Katz, A., 2013. Effect of particle diameter and surface composition on the spontaneous fusion of monolayer-protected gold nanoparticles with lipid bilayers. Nano Letters 13, 4060–4067.
Vacha, R., Martinez-Veracoechea, F.J., Frenkel, D., 2011. Receptor-mediated endocytosis of nanoparticles f various shapes. Nano Lett 11, 5391–5395.
Ruiz-Herrero, T., Velasco, E., Hagan, M.F., 2012. Mechanisms of budding of nanoscale particles through lipid bilayers. J. Phys. Chem. B 116, 9595–9603.
Spangler, E.J., Upreti, S., Laradji, M., 2016. Partial wrapping and spontaneous endocytosis of spherical nanoparticles by tensionless lipid membranes. J. Chem. Phys 144, 044901.
Proskar, P.A., Jameson, C.J., Murad, S., 2016. Simulated permeation and characterization of PEGylated gold nanoparticles in a lipid bilayer system. Langmuir 32, 7541–7555.
Koltover, J., Rädler, J.O., Safinya, C.R., 1999. Membrane mediated attraction and ordered aggregation of colloidal particles bound to giant phospholipid vesicles. Phys. Rev. Lett. 82, 1991–1994.
Sarfati, R., Dufresne, E.R., 2016. Long-range attraction of particles adhered to lipid vesicles. Phys. Rev E 94, 012604.
van der Wel, C., Vahid, A., Saric, A., Idema, T., Heinrich, D., Kraft, D.J., 2016. Lipid membrane-mediated attraction between curvature inducing objects. Scientific Rep 6, 32825.
Sugikawa, K., Kadota, T., Yasuhara, K., Ikeda, A., 2016. Anisotropic self-assembly of citrate-coated gold nanoparticles on fluidic liposomes. Angew. Chem. Int. Ed 55, 4059–4063.
Barbul, A., Singh, K., Horev-Azaria, L., Dasgupta, S., Auth, T., Korkenstein, R., Gompper, G., 2018. Nanoparticles-decorated erythrocytes reveal that particle size controls the extent of adsorption, cell shape and cell deformability. ACS Appl. Nano Mater. 1, 3785–3799.
Hooper, H.J., Schweizer, K.S., 2006. Theory of phase separation in polymer nanocomposites. Macromolecules 39, 5133–5142.
Ackora, P., Liu, H., Kumar, S.K., Moll, J., Li, Y., Benivewicz, B.C., Schadler, L.S., Acehan, D., Panagiotopoulos, A.Z., Priyamitsyn, V., Ganesan, V., Ilvasky, J., Thiyagarajan, P., Colby, R.H., Douglas, J.F., 2009. Anisotropic self-assembly of spherical polymer-grafted nanoparticles. Nature Mat. 8, 354–359.
Lopes, W.A., Jaeger, H.M., 2001. Hierarchical self-assembly of metal nanostructures on diblock copolymer scaffolds. Nature 414, 735–738.
Kang, S., Ryu, D.Y., Ringe, E., Hickey, R.J., Park, S.-J., 2020. Nanoparticle-induced self-assembly of block copolymers into nanoporous films at the air-water interface. ACS Nano 14, 12203–12209.
Jia, H., Bai, X., Li, N., Yu, L., Zheng, L., 2011. Siloxane surfactant induced self-assembly of gold nanoparticles and their application to SERS. Cryst. Eng. Comm 13, 6179–6184.
Rahimi, M., Roberts, T.F., Armas-Perez, J.C., Wang, X., Bukusoglu, E., Abbott, N.L., de Pablo, J.J., 2015. Nanpoarticle self-assembly at the interface of liquid crystal droplets. PNAS 112, 5297–5302.
Niu, Z., He, J., Russel, T.P., Wang, Q., 2010. Synthesis of nano/microstructures at fluid interfaces. Angew. Chem. Int. Ed. 49, 10052–10066.
Goulian, M., Bruisma, R., Pincus, P., 1993. Long-range forces in heterogeneous fluid membranes. Europhys. Lett 22, 145–150.
Golestanian, T., Goulian, M., Kardar, M., 1996. Fluctuation-induced interactions between rods on a membrane. Phys Rev. E 54, 6725–6734.
Park, J.M., Lubensky, T.C., 1996. Interactions between membrane inclusions on fluctuating membranes. J. Phys. I 6, 1217–1235.
Weikl, T.R., Kozlov, M.M., Helfrich, W., 1998. Interaction of conical membrane inclusions: Effect of lateral tension. Phys. Rev. E 57, 6988–6995.
Evans, A.R., Turner, M.S., Sens, P., 2003. Interactions between proteins bound to biomembranes. Phys. Rev. E 67, 041907.
Yolcu, C., Rothstein, I.Z., Deserno, M., 2012. Effective field theory approach to fluctuation-induced forces between colloids at an interface. Phys. Rev. E 85, 011140.
Ramakrishnan, N., Sunil Kumar, P.B., Ipsen, J.H., 2013. Membrane-mediated aggregation of curvature-inducing nematogens and membrane tubulation. Biophys. J 104, 1018–1028.
Reynwar, B.J., Illya, G., Harmandaris, V.A., Müller, M.M., Kremer, K., Deserno, M., 2007. Aggregation and vesiculation of membrane proteins by curvature-mediated interactions. Nature 447, 461–464.
Olinger, A.D., Spangler, E.J., Sunil Kumar, P.B., Laradji, M., 2016. Membrane-mediated aggregation of anisotropically curved nanoparticles. Faraday Discuss 186, 265–275.
Angelikopoulos, P., Sarkisov, L., Courinia, Z., Gkeka, P., 2017. Self-assembly of anionic, ligand-coated nanoparticles in lipid membranes. Nanoscale 9, 1040–1048.
Xiong, K., Zhao, J., Yang, D., Cheng, Q., Wang, J., Ji, H., 2017. Cooperative wrapping of nanoparticles of various sizes and shapes by lipid membranes. Soft Matter 13, 4644–4652.
Spangler, E.J., Sunil Kumar, P.B., Laradji, M., 2018. Stability of membrane-induced self-assemblies of spherical nanoparticles. Soft Matter 14, 5019–5030.
Revalee, J.D., Laradji, M., Sunil Kumar, P.B., 2008. Implicit-solvent mesoscale model based on soft-core potentials for self-assembled lipid membranes. J. Chem. Phys 128, 035102.
Laradji, M., Sunil Kumar, P.B., Spangler, E.J., 2016. Exploring large-scale phenomena in composite membranes through an efficient implicit solvent model. J. Phys. D: Appl. Phys 49, 293001.

Spangler, E.J., Laradji, M., 2020. Discontinuous wrapping transition of spherical nanoparticles by tensionless lipid membranes. J. Chem. Phys 152, 104902.
Hore, M.J.A., Laradji, M., 2007. Microphase separation induced by interfacial segregation of isotropic, spherical nanoparticles. J. Chem. Phys 126, 244903.
Hore, M.J.A., Laradji, M., 2008. Prospects of nanorods as an emulsifying agent of immiscible fluids. J. Chem. Phys 128, 054901.
Le Bihan, O., Bonnafous, P., Marak, L., Bickel, T., Trépout, S., Mornet, S., De Haas, F., Talbot, H., Taveau, J.-C., Lambert, O., 2009. Cryo-electron tomography of nanoparticle transmigration into liposome. J. Struct. Biol. 168, 419–425.
Van Lehn, R.C., Alexander-Katz, A., 2019. Energy landscape for the insertion of amphiphilic nanoparticles into lipid membranes: A computational study. PLOS One 14, e0209492.
Ting, C.L., Wang, Z.-G., 2012. Minimum free energy paths for a nanoparticle crossing the lipid membrane. Soft Matter 8, 12066.
Sunil Kumar, P.B., Rao, M., 1998. Shape Instabilities in the Dynamics of a Two-Component Fluid Membrane. Phys. Rev. Lett 80, 2489–2492.
Kumar, S., Bouzida, D., Swendsen, R.H., Kollman, P.A., Rosenberg, J.M., 1992. The weighted histogram analysis method for free-energy calculations on biomolecules. I. The method. Comput. Chem. 13, 1011–1021.
Humphrey, W., Drake, A., Schulten, K., 1996. VMD: Visual Molecular Dynamics. J. Mol. Graphics 14, 33–38.